

COHERENT DENSE CORES. I. NH₃ OBSERVATIONS

JOSEPH A. BARRANCO¹

Astronomy Department, University of California, Berkeley, Berkeley, CA 94720; jbaranco@astro.berkeley.edu

AND

ALYSSA A. GOODMAN²

Astronomy Department, Harvard University, Cambridge, MA 02138; agoodman@cfa.harvard.edu

Received 1997 April 30; accepted 1998 February 5

ABSTRACT

In a study of the velocity dispersion of molecular gas in NH₃ maps of four dense cores, we find that: (1) within the interiors of dense cores, the line widths are roughly constant at a value slightly but significantly higher than a purely thermal line width; and (2) at the edges of the maps of the dense cores, it appears that the line width starts to increase. We suggest that these dense cores are “coherent” in that the nonthermal, turbulent, contributions to the line width are so small that observed velocity dispersion is nearly independent of scale within the cores. In the second paper of this series (Goodman et al.), by analyzing maps of the cores’ environments, we find an apparent transition to this coherent regime from a more turbulent one, at about the size scale of a FWHM NH₃ contour, or ~ 0.1 pc.

Analysis of velocity gradients in dense cores and their environs indicates that the cores appear to spin independently of their surroundings, along an axis not obviously related to their shape. Comparison of gradients implied by the relative velocities of high-density cores in complexes and gradients in the extended low-density gas in these complexes suggests a picture in which the coherent cores behave as (independently spinning) test particles, floating along in a turbulent flow.

An appendix to this paper presents a new algorithm for predicting the intrinsic width of the 18 hyperfine lines in the NH₃ inversion spectrum from a Gaussian fit to the main hyperfine blend and an estimate of the optical depth.

Subject headings: ISM: clouds — ISM: kinematics and dynamics — ISM: molecules — ISM: structure — turbulence

1. INTRODUCTION

We began this project by asking ourselves the following question: Given that molecular clouds appear self-similar or “fractal” when mapped at higher and higher resolutions but that the stars forming within the clouds are clearly nonfractal discrete objects, can we find a scale on which pieces of molecular clouds lose their self-similarity and become “blobs” destined to form a single star or a very small group of stars? We investigated two approaches to this problem. On one hand, we could look directly at the structure of very dense gas, or, on the other hand, we could look at the cloud structure indirectly, by analyzing line width–size relations. It turns out to be very difficult to use the first approach and very fruitful to use the second. This paper and its companion (Goodman et al. 1998; hereafter, Paper II) describe how line width–size relations can be used to identify what we term “coherent cores”³ in the interstellar medium.

After analyzing line width–size relations derived from spectral line maps of *individual* molecular lines in *individual* molecular clouds, we propose that there is a ~ 0.1 pc scale characteristic of coherence, where turbulent cloud support dissipates to the point where self-gravitational energy can

exceed outward pressure, allowing cores to collapse, or fragment and then collapse, into protostars. We suspect that this dissipation of turbulence is related to a decoupling of the magnetic field from the neutral gas, which is caused by a reduced ionization fraction in these dense, high filling factor cores.

1.1. Historical Context

Within most dark interstellar clouds, there are small (0.1–0.4 pc), dense (10^4 – 10^5 cm⁻³) condensations of molecular gas known as low-mass dense cores (Myers & Benson 1983; Benson & Myers 1989), which often harbor pointlike embedded sources with protostellar-type spectra (Beichman et al. 1986). It is now widely believed that such cores, whose masses range from about 0.3–10 M_{\odot} , are capable of forming stars like the Sun when their innards become dense and compact enough to collapse under their own weight (see Shu 1995, and references therein).

On large scales, observed spectral line widths indicate that motions in the molecular clouds that harbor dense cores are highly supersonic (e.g., Barrett, Meeks, & Weinreb 1964). The supersonic or nonthermal portion of the line width is thought to arise from chaotic, wavelike, and/or turbulent motions. Suggestive evidence for turbulence was found by Larson (1981), who compiled data for many molecular clouds and condensations (with sizes between 0.1 and 100 pc) and showed that the internal velocity dispersion of each region is well correlated with its size and that this correlation is well approximated by a power law of the form $\Delta v \sim R^{a_1}$, with $a_1 = 0.38$. Larson noted that this correlation is very similar to the Kolmogorov law for subsonic incom-

¹ National Science Foundation Graduate Fellow.

² National Science Foundation Young Investigator.

³ We use the term “coherent” when referring to regions in which the observed velocity dispersion in the gas is roughly constant. We sometimes call these cores “velocity coherent,” not because every spectrum peaks at the same velocity, but because their “coherence” is most recognizable when analyzing velocity information (e.g., line widths).

pressible turbulence, which has a power-law index of $\frac{1}{3}$, suggesting that the observed motions could arise from a cascade of eddies from large scales down to small scales.

Additional evidence for turbulence has been found by calculating the autocorrelation and structure functions of velocity fields derived from spectral line maps of dark clouds (e.g., Kleiner & Dickman 1987; Kitamura et al. 1993; Miesch & Bally 1994). This method was first applied to molecular spectral line maps by J. Scalo in 1984. Scalo's study and the subsequent ones of this type primarily agree that turbulence is present in dark clouds but strongly disagree as to whether or not physically meaningful "correlation lengths" or other break points in the turbulence have been found (see § 5).

Although turbulence in the highly compressible interstellar medium (ISM) may be morphologically similar to Kolmogorov turbulence in an incompressible fluid, its physical origins and nature are still uncertain. Given that observed line widths are much larger than the sound speed but very close to the Alfvén speed in much of the ISM, it is has often been suggested that magnetic fields and their corresponding waves and instabilities play an important mitigating role in interstellar turbulence (e.g., Arons & Max 1975; McKee & Zweibel 1995; Zweibel & Josafatsson 1983). Recently, numerical simulations of the magneto-hydrodynamics of "magnetized molecular clouds" have become computationally feasible, and these simulations are producing structures that resemble real dark-cloud regions (e.g., Gammie & Ostriker 1996; Gammie, Stone, & Ostriker 1998).

In his 1981 study, Larson showed that the observed line width–size and density–size relations imply that (self-gravitating) clouds are close to virial equilibrium. Myers & Goodman (1988a, 1988b) extended Larson's work to show that if one assumes that magnetic fields limit the non-thermal line widths to be approximately the Alfvén speed, then Larson-like line width–size relations can be explained as the result of equipartition among kinetic, magnetic, and gravitational energy (see also McKee & Zweibel 1995). Thus, our current picture of the nonthermal line widths is that they originate in magnetized, turbulent gas and that they are crucial to the support of molecular clouds on scales at which the nonthermal line width dominates the thermal line width.

1.1.1. Types of Line Width–Size Relations

Larson's 1981 study includes line width and size observations for many different clouds, observed in a variety of different spectral lines or "tracers." In Paper II, we put Larson's study into context by defining and discussing four distinct "Types" of line width–size relation.⁴ In this paper, we only need to point out that there are important physical differences between: multitracer-multicloud (Type 1); single-tracer-multicloud (Type 2); multitracer-single-cloud (Type 3); and single-tracer-single-cloud (Type 4) line width–size relations. Each Type i of line width–size relation uses a different method for measuring line width and size, but each can give $\Delta v \propto R^{a_i}$. In the literature to date, line width–size relations of all Types are often used interchangeably, especially in data-theory comparisons.

TABLE 1
TYPES OF LINE WIDTH–SIZE RELATION

	Multiple Tracers	Single Tracer
Multiple Clouds	1	2
Single Cloud	3	4

It is physically unlikely that $a_1 = a_2 = a_3 = a_4$. Many single-tracer, multicloud (Type 2) studies find correlations with a power-law index $a_2 \approx 0.5$ (e.g., Leung, Kutner, & Mead 1982; Torrelles et al. 1983; Dame et al. 1986; Scoville, Sanders, & Clemens 1986; Solomon et al. 1987). An index of $a_2 = 0.5$ is automatically predicted for a tracer of constant column density in clouds that are close to virial equilibrium, so this exponent may not reveal much about the detailed internal dynamics of the clouds. Multitracer, single-cloud (Type 3) relations, which can sample a wide range of densities by using a wide variety of tracers to observe a single region, give the best indication of the pressure structure within an individual cloud. Typically, Type 3 studies on sub-parsec scales find power-law indices $0.25 < a_3 < 0.75$ (Martin & Barrett 1978; Myers et al. 1978; Snell 1981; Caselli & Myers 1995; Fuller & Myers 1992; Myers & Fuller 1992). In Paper II, we suggest that Type 3 relations should flatten out at small size scales, where the line widths are nearly thermal. As a result, we predict a *bend* in the Type 3 relation, which means that the exact slope of a single power-law fit will depend, in part, on the range of densities observed. Thus, the observed wide range of single power-law Type 3 slopes is expected. In multitracer, multicloud (Type 1) studies, such as Larson's, line width and size measurements for many different clouds, observed in many different tracers, are fit simultaneously, which yields a power law with slope $0.4 \lesssim a_1 \lesssim 0.5$ for low-density clouds (e.g., Larson 1981) and $a_1 \sim 0.2$ for dense cores⁵ (Fuller & Myers 1992). Type 1 studies typically include a large number of observations, so a_1 can be determined very accurately. However, even after accounting for measurement error, the scatter in these Type 1 relations is very significant, and it is likely indicative of the real region-to-region scatter in the physical conditions in the ISM.

Since a cloud's velocity dispersion cannot fall below the sound speed, the line width–size correlation should not continue unchanged to ever-decreasing size scales. Indeed, in his original paper, Larson (1981) suggests that the line width–size power law might end with objects so small that their internal motions are no longer supersonic: a purely thermal ball of gas would have no dependence of velocity dispersion on size, i.e., $a_i = 0$. The subtle question, though, is what subscript, i , to put on that a_i . In a Type 1 (multitracer, multicloud) study of relatively high-density objects, Myers (1983) finds that the nonthermal component of the velocity dispersion continues to decrease with decreasing size ($a_1 > 0$), even for cases in which the total velocity dispersion is almost thermal (dense cores). And, in Type 3 (multitracer, single-cloud) studies, Fuller & Myers (1992) and Caselli & Myers (1995) find that the line widths of tracers with decreasing half-power radii also continue to decrease ($a_3 > 0$), even inside dense cores whose line width is primarily thermal (see Paper II). In both of these Type 1

⁴ A table from Paper II summarizing the four Types is reproduced here as Table 1. Figure 7 of Paper II gives a graphical summary of the Types.

⁵ This slope is for the relation between the total (thermal plus nonthermal) line width and the size. For the nonthermal component alone, Fuller & Myers (1992) find $\Delta v_{NT} \propto R^{0.7}$.

and Type 3 relations, subtle but suggestive changes in slope may be associated with a transition to a thermally dominated region, but the transition point is not entirely clear. We seek a new kind of line width–size relation that might be more sensitive to the nonthermal/thermal transition that Larson originally envisioned.

1.1.2. *The Current Study: Type 4 Relations and Coherence*

This paper and Paper II present studies of Type 4 line width–size relations: *the dependence of line width on size scale in individual clouds observed in individual tracers*. Line width–size relations for single regions mapped in single tracers have been examined in lower density gas by Miesch & Bally (1994) and by Heyer & Schloerb (1997), but the small size of dense cores has caused them to be excluded from such studies in the past. The line width–size relations produced in the published lower density single-tracer studies can be thought of as Type 4 if the regions studied can legitimately be regarded as single clouds. In this paper, we analyze (§ 3) very sensitive observations (§ 2) of NH_3 in dense cores, which we find correspond to a coherent regime in which $a_4 \rightarrow 0$. We find (§§ 4 and 5) that the almost constant line width within the cores is mildly but significantly *supersonic* so that a “coherent dense core” is similar to, but not exactly the same as, an isothermal ball of gas. Furthermore, in cases in which velocity gradients can be determined for a core and its “environment” from a single large map, we point out (§ 4.2) that the cores usually have a distinct implied rotation axis from their surroundings.

In Paper II, we present observations of the lower density gas surrounding the cores, which allows us to compare single-tracer, single-cloud (Type 4) line width–size relations across density regimes. We find that the value of a_4 depends on the average density associated with the tracer observed. For low densities ($\lesssim 10^2$), $a_4 \rightarrow a_2 \approx 0.5$, and for high densities ($\gtrsim 10^4$), $a_4 \rightarrow 0$. We propose that the regime in which $a_4 \rightarrow 0$ corresponds to size scales (~ 0.1 pc) on which low-mass star formation takes place—coherent dense core size scales. Furthermore, we propose an underlying physical relationship between line width and size that can self-consistently explain the slopes of all of the observed types of line width–size relations. This underlying relationship includes a “transition to coherence” at $R_{\text{coh}} \approx 0.1$ pc, which is most likely caused by significant slippage of magnetic fields inside clouds with average density greater than 10^4 in low-mass star-forming regions.

2. OBSERVATIONS

In this paper, we present an analysis of the velocity structure for the dense cores L1495, TMC-1C, L43/RNO 90, and L1251A as observed in the $(J, K) = (1, 1)$ rotation inversion transition of NH_3 . Table 2 presents map data for each core. Spectral line maps for these cores were originally presented in Benson & Myers (1989). However, these maps typically extend only to the “half-power contour,” at which the measured antenna temperature falls to half the value of that at the peak of the map. In order to do a detailed analysis of the velocity structure, it was necessary to both redo some points on the edges of the maps at which the signal-to-noise ratio (S/N) was significantly less than 3 and to extend the maps beyond the half-power contour.

The spectral line maps from Benson & Myers (1989) were made during several observing sessions between 1981 and 1985 at the 37 m radio telescope at Haystack Observatory (L1251A, L43/RNO 90, and L1495) and at the 43 m radio telescope at the National Radio Astronomy Observatory (TMC-1C). The bandwidths used were 5.55 MHz at Haystack and 5.0 MHz at NRAO. The velocity resolutions of the spectra (1.21 times the channel spacing, for unity weighting in the time domain) were $0.08 \text{ km s}^{-1} \text{ channel}^{-1}$ at Haystack and $0.07 \text{ km s}^{-1} \text{ channel}^{-1}$ at NRAO. All data at both telescopes were taken in the overlapped frequency-switching mode by switching by 104 kHz. The spectra were corrected for atmospheric attenuation, and variation of gain with elevation (Haystack) or hour angle (NRAO). No determination was made of the beam efficiency, so the temperature scales are the antenna temperatures for each telescope.

We made additional observations to expand the maps for L1251A, L43/RNO 90, and L1495 at the 37 m radio telescope at Haystack Observatory in October 1993. The bandwidth used was 5.9 MHz, giving a channel spacing of 0.009 km s^{-1} . Spectra were taken in overlapped frequency-switching mode by switching by 376 kHz. Spectra were corrected for atmospheric attenuation and variation of gain with elevation. All spectra were folded after a third-order polynomial baseline was removed and then were boxcar smoothed by four channels, yielding a velocity resolution of $0.037 \text{ km s}^{-1} \text{ channel}^{-1}$. As with the Benson & Myers (1989) observations, we made no determination of the beam efficiency, so the temperature scale is the antenna temperature for the Haystack telescope.

TABLE 2
MAP DATA FOR CLOUD CORES

CORE	N^b	D (pc)	PEAK POSITION ^a		v_{LSR}^c (km s^{-1})	$\Delta v_{\text{blend}}^c$ (km s^{-1})	Δv_{int}^d (km s^{-1})	ROTATION ANGLE ^e (deg)	MAJOR AXIS ^f (arcmin)	MINOR AXIS ^f (arcmin)	AXIAL RATIO
			R.A. (1950)	Decl. (1950)							
L1495	59	140	04 11 07.4	28 01 58	6.8	0.67	0.24	125	5.4	2.7	2.0
TMC-1C	34	140	04 38 34.4	25 55 00	5.2	0.70	0.27	139	6.3	2.1	3.0
L43/RNO 90	55	160	16 31 43.4	−15 40 40	0.7	0.75	0.33	177	4.1	2.1	2.0
L1251A	35	200	22 30 20.3	74 57 51	−4.3	0.71	0.29	171	7.1	2.0	3.6

NOTE.—Information in this table is from Benson & Myers 1989.

^a (0, 0) positions for each map are given in the caption to Fig. 1.

^b N is the number of points (spectra) in the map with a S/N greater than about 3.

^c Line parameters from fitting single Gaussian to the main blend of the NH_3 $(J, K) = (1, 1)$ transition.

^d Intrinsic line width Δv_{int} from 18 component fitting using CLASS.

^e The rotation angle is defined as the angle (in a clockwise direction) between the major axis of the core and the positive right ascension axis.

^f The maps have been fitted to a two-dimensional Gaussian model to determine the half-power (FWHM) sizes.

TABLE 3
 Δv_{blend} TO Δv_{int} CONVERSION COEFFICIENTS, K_{nm}

m	n			
	0	1	2	3
0.....	-0.3308	0.8572	-0.1062	0.0152
1.....	-0.6072	1.8001	-0.9679	0.2179
2.....	0.1808	0.1932	0.2479	0.2950

For positions in the maps at which we had both new (1993) and old (1980s) data, the new spectra were smoothed to the resolution of the old spectra, and then they were averaged, with weights proportional to the inverse of the square of the root mean square (rms) noise: $w \sim \sigma_{\text{rms}}^{-2}$.

3. DATA ANALYSIS

3.1. Line Fitting with CLASS

All spectral line fitting was done with the CLASS software package (Forveille, Guilloteau, & Lucas 1989). The “main blend,” which consists of the central eight hyperfine components of the NH_3 (J, K) = (1, 1) transition, was fit with a single Gaussian profile by a nonlinear, least-squares method, yielding three fit parameters for each spectrum: a peak antenna temperature T_A^* , a line-of-sight velocity v_{LSR} , and a blended line width (FWHM) Δv_{blend} . Statistical uncertainties in each of the fit parameters were computed using the analytic formulae derived by Landman, Roussel-Dupré, & Tanigawa (1982):

$$\sigma_{T_A^*} = 1.41 \left(\frac{\delta_v}{\Delta v} \right)^{1/2} \sigma_{\text{rms}}, \quad (1)$$

$$\sigma_{v_{\text{LSR}}} = 0.69 (\delta_v \Delta v)^{1/2} \frac{\sigma_{\text{rms}}}{T_A^*}, \quad (2)$$

and

$$\sigma_{\Delta v} = 1.63 (\delta_v \Delta v)^{1/2} \frac{\sigma_{\text{rms}}}{T_A^*}, \quad (3)$$

where δ_v is the velocity resolution and σ_{rms} is the rms noise in the spectrum.

In cases in which the S/N was greater than about 4 or 5, we also used CLASS to perform a more sophisticated nonlinear, least-squares fit to all 18 hyperfine components simultaneously, thus allowing for a determination of the total optical depth τ_0 and the intrinsic line width (FWHM) Δv_{int} of the spectrum (Forveille et al. 1989; Benson & Myers 1989; Bachiller, Guilloteau, & Kahane 1987; Pauls et al. 1983). The method assumes that each hyperfine component has a fraction of the total optical depth based on its theoretical percentage of the line (Kukolich 1967) and has the same excitation temperature and intrinsic line width. Statistical uncertainties for the 18 component fits were computed by the gradient method within CLASS.

3.2. Converting Main-Blend Line Width to Intrinsic Line Width

In order to derive accurate estimates of the intrinsic width of the 18 hyperfine lines in the NH_3 inversion spectrum, it was necessary to develop a procedure to convert main-blend (also known as “blended”) line widths to intrinsic line widths for those spectra in which we could not fit all 18 components simultaneously, either because the spectra had insufficient S/N or because we did not have access to the original spectra (as was the case for some of the Benson & Myers 1989 data). To create a conversion algorithm, we simulated ammonia spectra with different intrinsic line widths and optical depths and then fit single Gaussians to the resulting main blends. From the simulations, we extracted an empirical relation for intrinsic line width as a function of main-blend line width and total optical depth. Appendix A presents the details of this procedure. Ultimately, we find that the intrinsic NH_3 line width can be expressed as a third-order polynomial of the main-blend line width and that the polynomial coefficients depend exponentially on the total optical depth:

$$\Delta v_{\text{int}} = \sum_{n=0}^3 C_n(\tau_0) \Delta v_{\text{blend}}^n, \quad (4)$$

$$C_n(\tau_0) = K_{n0} + K_{n1} \exp(-K_{n2} \tau_0), \quad (5)$$

where the values of the coefficients K_{nm} can be found in Table 3. The relation does not depend strongly on the total optical depth; in general, even a 33% uncertainty in τ_0 results in no more than a 10% uncertainty in Δv_{int} . The largest contribution to the error in the intrinsic line width is the error in the blended line width; a 5% error in Δv_{blend} typically results in a 10% error in Δv_{int} .

3.3. Velocity Gradient Fitting

Any component of solid-body rotation in a molecular cloud will produce a linear gradient, ∇v_{LSR} , in the LSR velocity field, along a direction perpendicular to the rotation axis, ω . Using the program VFIT, developed by Goodman et al. (1993), we fit the function

$$v_{\text{LSR}} = v_0 + a \Delta \alpha + b \Delta \delta \quad (6)$$

to the velocity fields observed in the spectral line maps of each of the four dense cores. Here, $\Delta \alpha$ and $\Delta \delta$ represent offsets in right ascension and declination, a and b are the projections of the gradient on the α and δ axes, and v_0 is the systemic velocity of the cloud with respect to the local standard of rest. The magnitude of the velocity gradient, in a cloud at distance D , is

$$\mathcal{G} \equiv |\nabla v_{\text{LSR}}| = \frac{\sqrt{a^2 + b^2}}{D}, \quad (7)$$

FIG. 1.—Maps of four dense cores [epoch 1950 (0, 0) positions listed in parentheses]: (a) L1495 ($04^{\text{h}}10^{\text{m}}49^{\text{s}}.3$, $28^{\circ}03'58''$), (b) TMC-1C ($04^{\text{h}}38^{\text{m}}34^{\text{s}}.5$, $25^{\circ}55'00''$), (c) L43/RNO 90 ($16^{\text{h}}31^{\text{m}}18^{\text{s}}.5$, $-15^{\circ}41'40''$), (d) L1251A ($22^{\text{h}}29^{\text{m}}03^{\text{s}}.2$, $74^{\circ}58'51''$). Solid-line contours delineate the core, showing peak antenna temperature T_A^* as determined by single-Gaussian fits to the spectrum taken at each position. Lighter shading indicates smaller values, and darker shading indicates larger values. Notice that not all maps span the full white-to-black range of gray scale available, and Fig. 3 gives a better indication of the exact range of each data set. For each source, the heavy solid contour is the half-power contour and is listed in boldface below. The contour levels for T_A^* and gray scale ranges (white-to-black) for the v_{LSR} and Δv_{int} panels are as follows. L1495: $T_A^* = 0.25, \mathbf{0.4}, 0.55, 0.7$ K; $6.2 \leq v_{\text{LSR}} \leq 6.8$ km s $^{-1}$ in steps of 0.1 km s $^{-1}$; $0.1 \leq \Delta v_{\text{int}} \leq 0.8$ km s $^{-1}$ in steps of 0.2 km s $^{-1}$. TMC-1C: $T_A^* = 0.25, \mathbf{0.4}, 0.55, 0.7$ K; $5 \leq v_{\text{LSR}} \leq 5.6$ km s $^{-1}$ in steps of 0.1 km s $^{-1}$; $0.15 \leq \Delta v_{\text{int}} \leq 0.45$ km s $^{-1}$ in steps of 0.05 km s $^{-1}$. L43/RNO 90: $T_A^* = 0.4, \mathbf{0.7}, 1.0, 1.3$ K; $0.3 \leq v_{\text{LSR}} \leq 0.8$ km s $^{-1}$ in steps of 0.1 km s $^{-1}$; $0.1 \leq \Delta v_{\text{int}} \leq 0.7$ km s $^{-1}$ in steps of 0.15 km s $^{-1}$. L1251A: $T_A^* = 0.25, \mathbf{0.4}, 0.55, 0.7$ K; $-4.4 \leq v_{\text{LSR}} \leq -3.8$ km s $^{-1}$ in steps of 0.1 km s $^{-1}$; $0.15 \leq \Delta v_{\text{int}} \leq 0.45$ km s $^{-1}$ in steps of 0.02 km s $^{-1}$. Positions and properties for the embedded protostars associated with these cores can be found in Benson & Myers (1989).

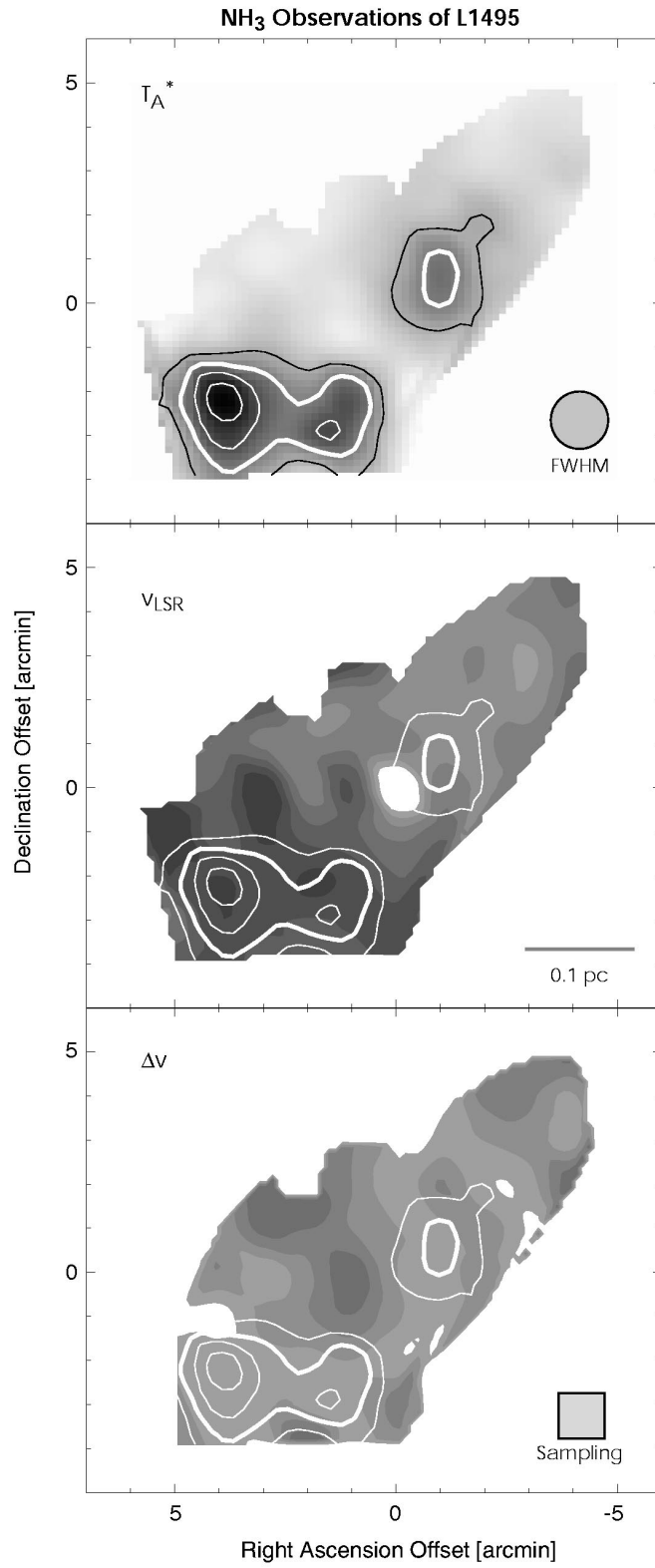


FIG. 1a

NH₃ Observations of TMC-1C

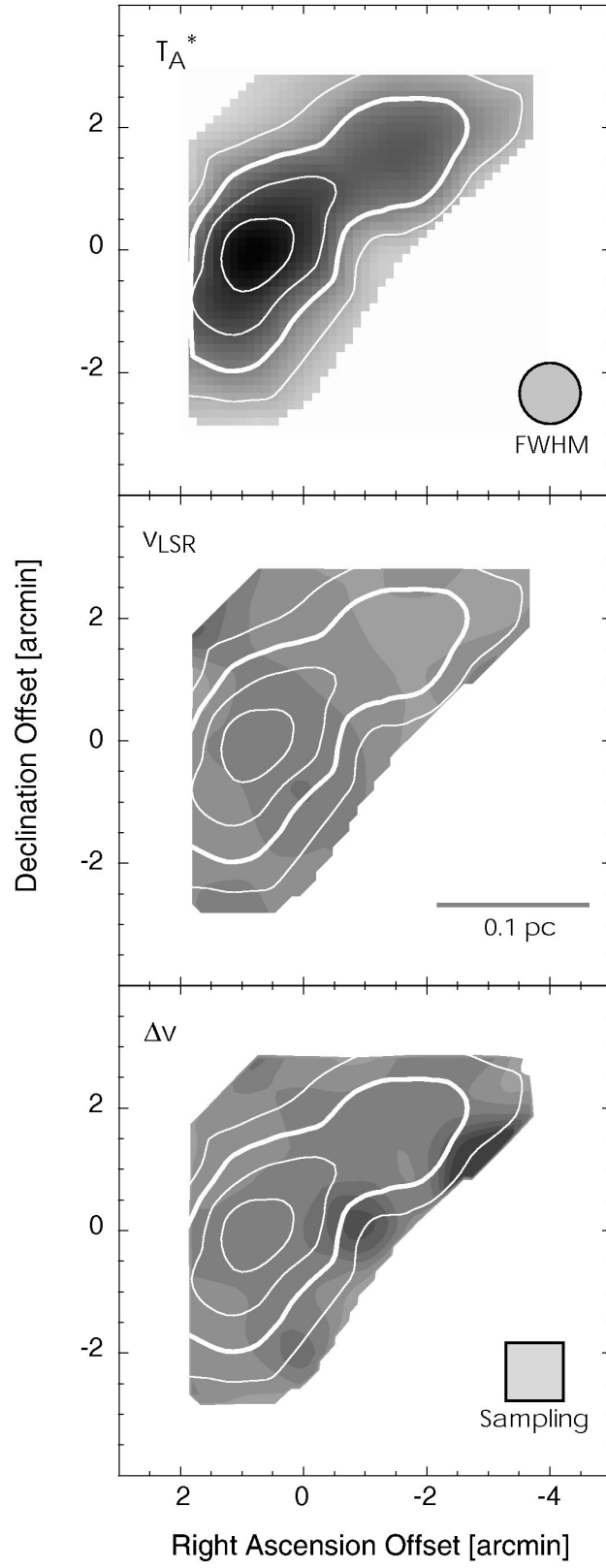


FIG. 1b

NH₃ Observations of L43/RNO90

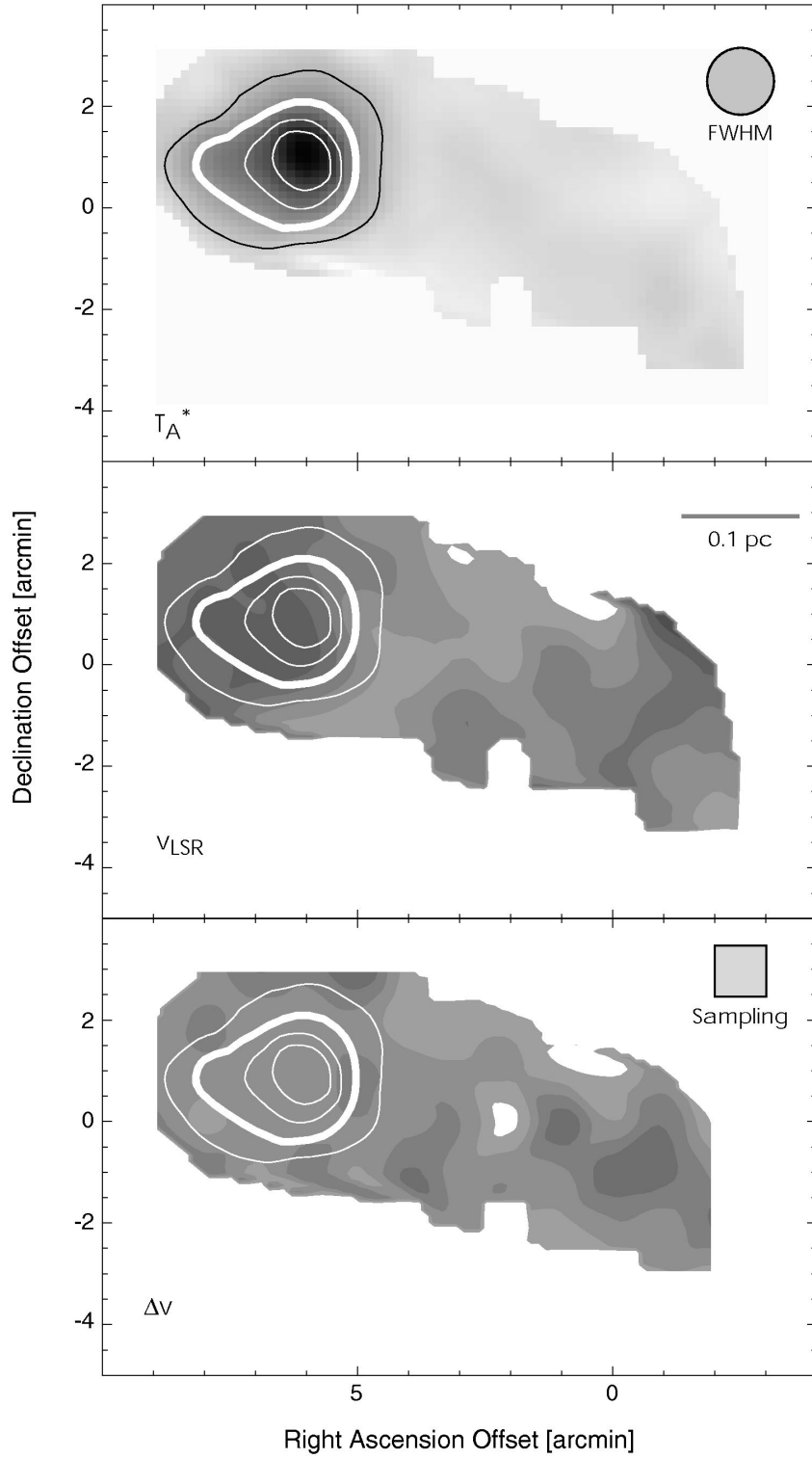


FIG. 1c

NH₃ Observations of L1251A

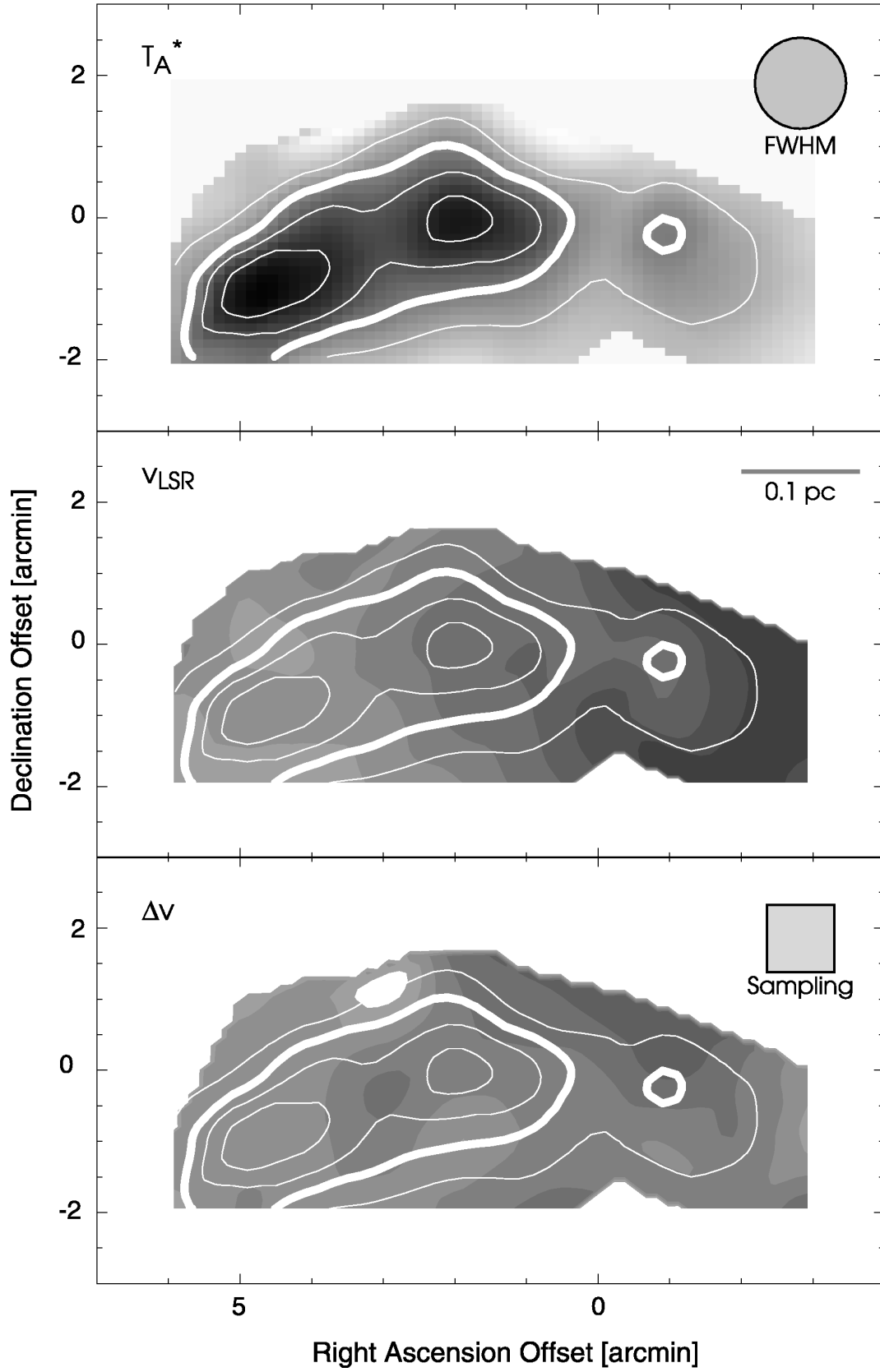


FIG. 1d

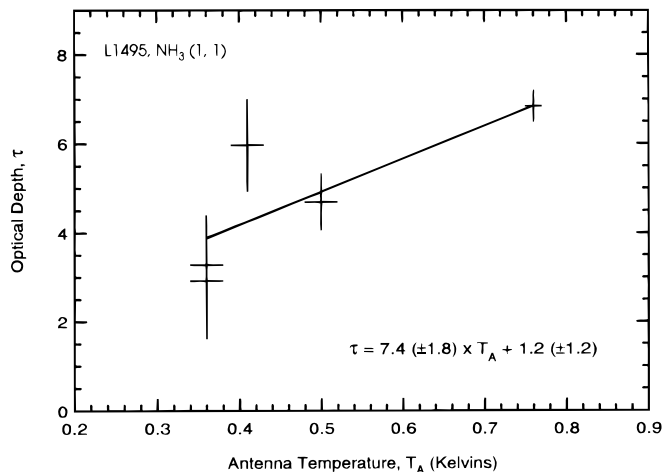


FIG. 2a

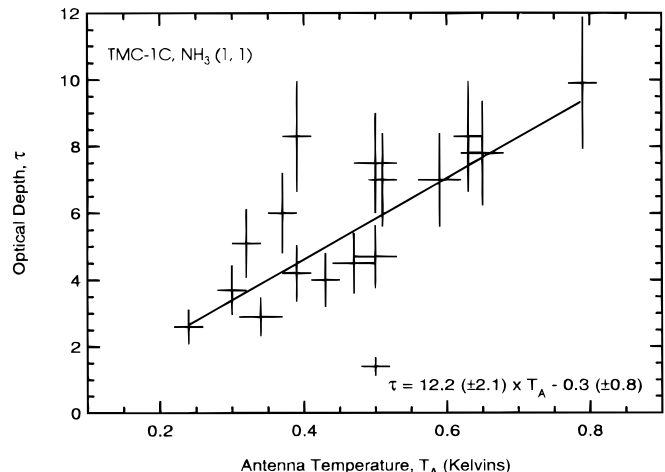


FIG. 2b

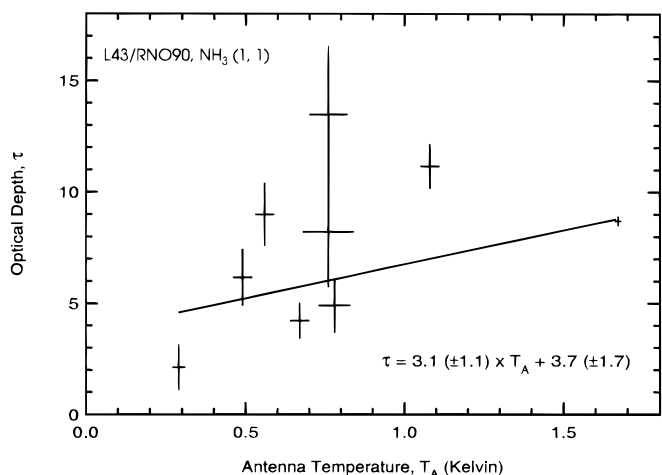


FIG. 2c

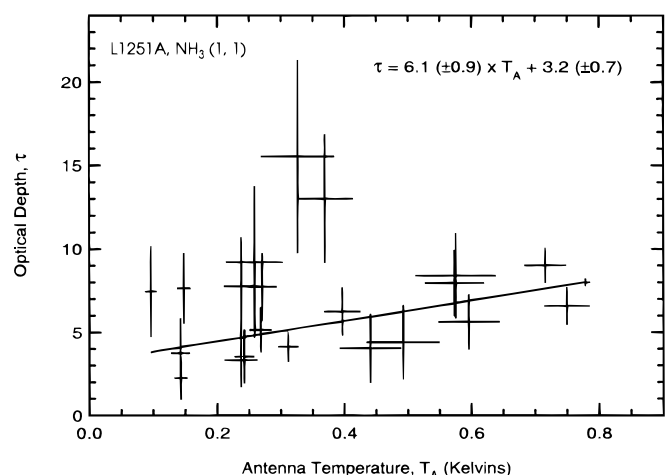


FIG. 2d

FIG. 2.—Total optical depth of the NH_3 (J, K) = (1, 1) transition as a function of antenna temperature T_A^* : (a) L1495, (b) TMC-1C, (c) L43/RNO 90, and (d) L1251A. Error bars indicate uncertainties. Linear (weighted) fits and errors are shown for each core.

and its direction (the direction of increasing velocity, measured east of north) is given by

$$\theta_{\mathcal{G}} = \tan^{-1}(a/b). \quad (8)$$

VFIT performs a least-squares fit of equation (6) with each v_{LSR} weighted by the reciprocal of the square of its uncertainty, $\sigma_{v_{\text{LSR}}}^{-2}$, calculated according to equation (2), and returns the magnitude of the gradient (\mathcal{G}), its direction ($\theta_{\mathcal{G}}$), and the errors in those quantities.

4. RESULTS

Maps of the velocity structure in the dense cores L1495, TMC-1C, L43/RNO 90, and L1251A are shown in Figure 1. Solid-line contours delineate the core, showing peak antenna temperature T_A^* as determined by single-Gaussian fits to the spectrum taken at each position. For each source, the heavy solid contour is the half-power contour, at which the antenna temperature has fallen to half its value at the peak of the map. Gray-scale shading in the top panel also shows T_A^* , while the gray scale in the middle panel shows LSR velocity, and the gray scale in the lower panel illustrates intrinsic line width Δv_{int} determined from 18 component fitting or from the technique described below. Lighter shading indicates smaller values, whereas darker shading indicates larger values.

In calculating the intrinsic line widths shown in Figure 1, we used the estimation technique described in § 3.2 for positions at which no 18 component fit to the NH_3 spectrum was possible. Recall that this technique uses the blended line width along with an estimate of the total optical depth to estimate intrinsic width. Since the total optical depth τ_0 is not measured at every position in our maps, we endeavored to find a predictive function $\tau_0(T_A^*)$ by using information from the positions at which both T_A^* and τ_0 are measured. Figure 2 plots τ_0 versus T_A^* for all spectra whose S/N allows for 18 component fitting.⁶ From these plots, we often see clear evidence for increases in τ_0 with T_A^* . The linear fits shown on the graphs were used as a best estimate of $\tau_0(T_A^*)$ in estimating the intrinsic widths shown in Figure 1. The scatter around these fits is large, but below (see § 4.1 and Fig. 4), we show that the results of this paper are not critically sensitive to the choice of the $\tau_0(T_A^*)$ relation.

4.1. Intrinsic Line Width versus Antenna Temperature

In Figure 1, there are hints of an interesting relation between intrinsic line width and position within each spec-

⁶ Note that τ_0 , plotted in Fig. 2, is the total optical depth for the sum of all 18 components. The optical depth in any single component is much less than τ_0 .

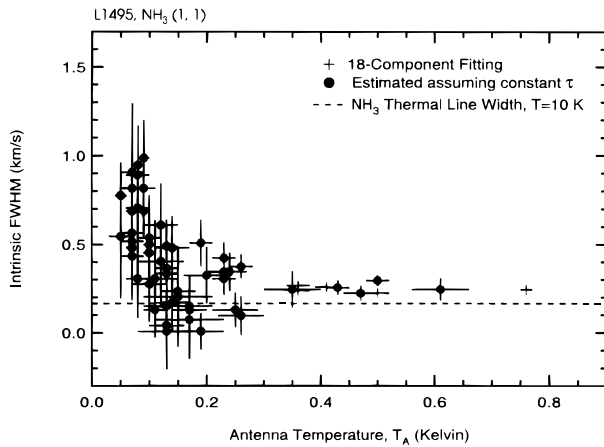


FIG. 3a

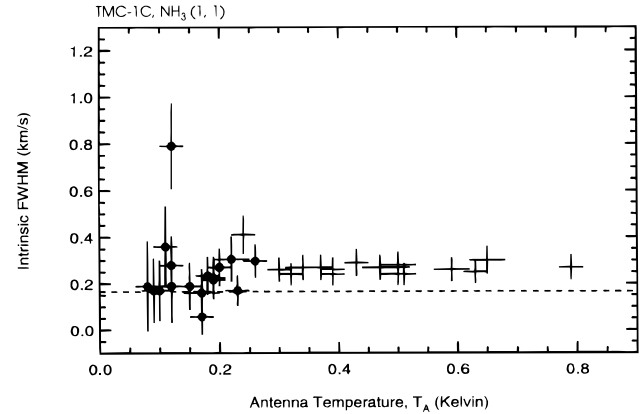


FIG. 3b

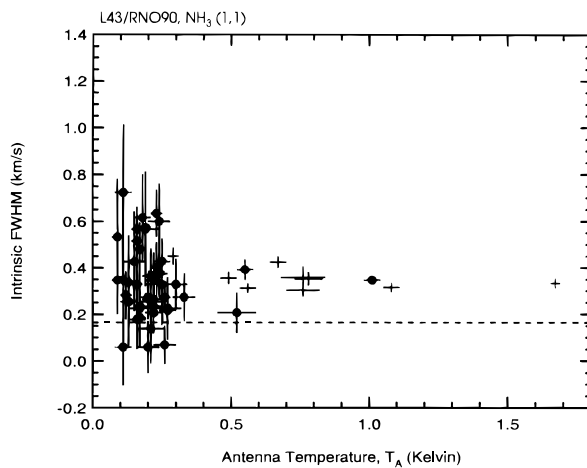


FIG. 3c

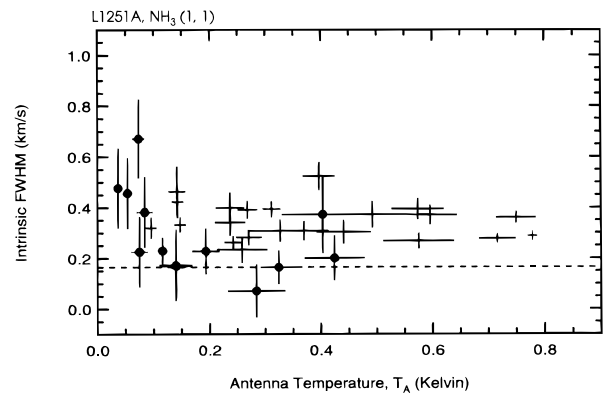


FIG. 3d

FIG. 3.—Intrinsic line width Δv_{int} vs. antenna temperature T_A^* : (a) L1495, (b) TMC-1C, (c) L43/RNO 90, and (d) L1251A. Error bars indicate uncertainties. Crosses mark line widths derived from simultaneously fitting all 18 components of the NH_3 (J, K) = (1, 1) transition. Circles mark line widths derived from employing the empirical relation in § 3.2 and using the linear relations between total optical depth τ_0 and T_A^* (see Fig. 2). The dashed line at 0.16 km s⁻¹ is the thermal line width for NH_3 , assuming $T_{\text{kinetic}} \approx 10$ K.

tral line map. There appears to be more scatter in the line width toward the edges of the map than toward the peak. Near the peaks, the line width seems to plateau at a value slightly greater than the thermal NH_3 FWHM line width of 0.16 km s⁻¹ (for $T_{\text{kinetic}} \approx 10$ K). However, from these figures, it is difficult to determine how much of the scatter at the edges of the map is inherent and how much is due to greater statistical uncertainty in the measurements given the lower S/N of the spectra of edge points. A better way to study this correlation is from a simple scatter plot of intrinsic line width versus antenna temperature.

We propose that plots of line width versus antenna temperature in dense core regions are essentially single-tracer, single-cloud (Type 4) line width–size relations. This equivalence is obvious in the case of a simple centrally peaked map, with one set of concentric contours. However, in cases in which map contours have irregular (nonellipsoidal) shapes, or if there are multiple peaks in a map, it is often difficult to unambiguously assign a physical “radius” to each position within a map. If a legitimately representative $T_A^*(R)$ function can be found, then a Δv – T_A^* relation can be transformed into a representative Δv – R relation without having to assign a size to each point in the map. For this reason, we choose to use antenna temperature as a proxy

for size in order to avoid assigning shapes to each core. In Appendix B, by fitting plots of T_A^* versus R , we show that a power law of the form $T_A^* \propto R^{-1}$ fits the data well in most NH_3 cores. Paper II examines tracer-to-tracer variations in this $T_A^*(R)$ relationship.

Figure 3 shows intrinsic line width versus antenna temperature for the four cores under consideration. As Figure 1 hinted, at high antenna temperatures (small radius), there is very little scatter in Δv_{int} . More specifically, it appears that the vast majority of points within the half-power contour have a nearly constant line width that is just slightly higher than the thermal line width. At low antenna temperatures (large radius, toward the edges of the maps), there is significantly more scatter in the line width, and the average line width is larger than that found within the half-power contours of the maps. To reduce the scatter in these plots in order to see the average behavior of the line width with antenna temperature, we have binned the data in bins of $T = 0.1$ K and averaged the line widths within each bin. In averaging, the line widths were weighted by the reciprocal of the squares of their uncertainties. The binned results (Fig. 4) again show Δv_{int} within the half-power contour of an ammonia core to be nearly independent of radius. In several cases, Figure 4 gives a slight indication that toward the

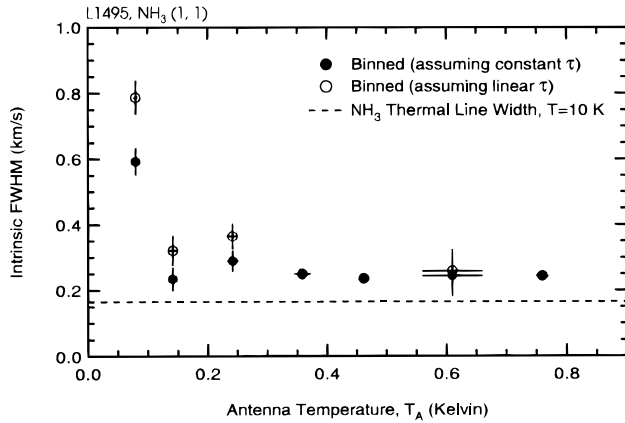


FIG. 4a

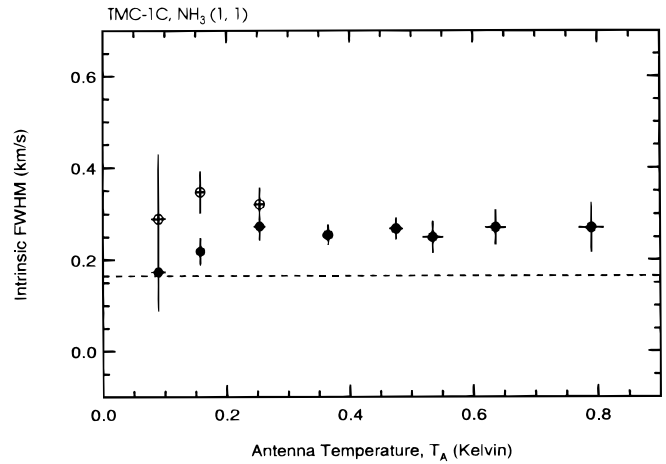


FIG. 4b

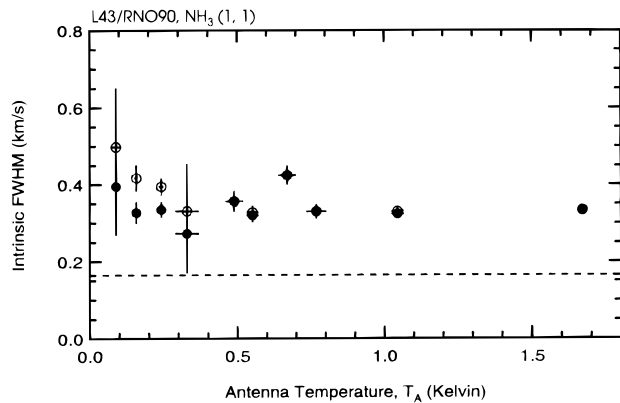


FIG. 4c

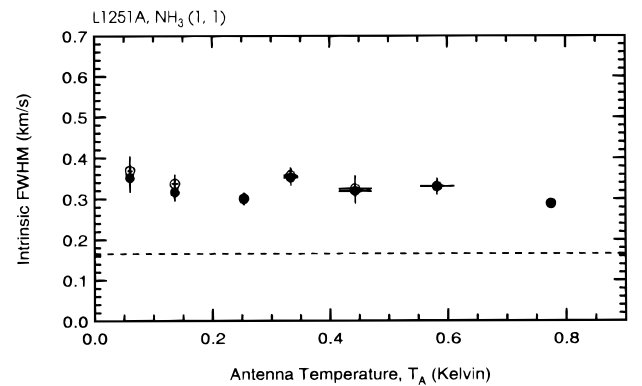


FIG. 4d

FIG. 4.—Same as in Fig. 3, but averaged in bins of width 0.1 K

edges of the maps, the average line is slightly broader. These general trends hold using either our best-fit $\tau_0-T_A^*$ relations or using an assumption of constant optical depth.

Examining Figure 4 carefully, one can envision two subtle modifications to the graphs that might change our conclusions. First, one can imagine assuming a value for the kinetic temperature and then plotting a calculated non-thermal line width instead of the observed intrinsic line width. This change magnifies any differences between the line width at large and small radii—if the observed line widths are close enough to thermal. We have constructed such plots (shown in Paper II), and we find that the thermal line width at 10 K (shown as a dashed line in Figs. 3 and 4) is a small enough fraction of the intrinsic width that this modification has virtually no effect. Indeed, one needs to hypothesize unreasonably high kinetic temperatures (~ 30 K) before Δv_{int} approaches a thermal width (see Paper II). Secondly, one might plot the $\Delta v_{\text{int}}-T_A^*$ data on a log-log scale, so that any power-law behavior is more easily detected. In Paper II, where we compare log-log plots of line width–size relations on many scales, we derive single power-law relations of the form $\Delta v_{\text{NT}} \propto R^{a_4}$ by combining power-law fits to $\Delta v_{\text{NT}}-T_A^*$ data (e.g., Fig. 4) and power-law fits to T_A^*-R data (e.g., Fig. 7). We find that the slope of these fits is ~ 0 within the half-power contour of the NH_3 maps (see Fig. 4) and only slightly larger ($a_4 \approx 0.1$) for fits includ-

ing data all the way down to the $\sim 10\%$ contour. In Paper II we find that, as a general rule, a_4 increases as the average density to which the observed tracer decreases and the scale over which that tracer is spread increases.

4.2. Gradients and Rotation

In a study of velocity gradients in dense cores, Goodman et al. (1993) find that in cases like L1251 and L43 in which the NH_3 map is extended enough to separate the core from its environment, the core often has a well-defined gradient along a direction distinct from another well-defined gradient in the surroundings. The most important result of the gradient analysis described below is that the additional data obtained for the present study continue to bear out this trend: cores often exhibit gradients oriented differently from those in their surroundings.

In Figure 1, one can see the smooth gradients in the LSR velocity fields across the face of the maps, which can be interpreted as solid-body rotation. (The gradients could also be caused by local shear in the velocity field, but we assume here that they are caused primarily by rotation.) Using the data sets depicted in Figure 1, we have recalculated the gradients and β -values for TMC-1C, L1495, L43/RNO 90, and L1251, which were originally calculated in Goodman et al. (1993), who used smaller data sets. Recall that the parameter β is a simple measure of the dynamical

TABLE 4
RESULTS OF GRADIENT FITTING

Core	\mathcal{G} (km s ⁻¹ pc ⁻¹)	Direction (deg east of north)	log n^a (cm ⁻³)	β
L1495	1.40 ± 0.07	132 ± 3	3.7	0.13
L1495NW	0.34 ± 0.20	158 ± 35	3.7	0.0074
L1495SE	0.48 ± 0.08	81 ± 15	3.7	0.015
TMC-1C	0.45 ± 0.09	122 ± 11	4.1	0.0052
L43/RNO 90	1.07 ± 0.05	108 ± 4	5.0	0.0037
L43	1.29 ± 0.10	92 ± 4	5.0	0.0053
L1251A	1.07 ± 0.02	-93 ± 6	4.1	0.029

^a Assuming $\sin i = 1$ and using values of the number density ρ_0 for the closest core listed in Benson & Myers 1989.

role of rotation and is defined as the ratio of rotational kinetic energy to gravitational potential energy. For a sphere with constant density ρ_0 , β is given by

$$\beta = \frac{1}{4\pi G\rho_0} \frac{\mathcal{G}}{\sin^2 i}, \quad (9)$$

where i is the inclination angle of the rotation axis $\hat{\omega}$ to the line of sight (Goodman et al. 1993). Table 4 lists the fitted gradient, along with a determination of β , for each core.⁷ Note that in the case of L1495, we fit the individual clumps (labeled NW and SE) separately as well as the whole cloud complex. For L43, we fit the individual core (defined by $T_A^* > 0.4$ K), the core plus its surroundings (the whole map shown in Fig. 1), and the surroundings “minus” the core (defined by $T_A^* < 0.4$). As in Goodman et al. (1993), comparison of the gradient position angles in the table shows that cores often rotate along a different axis than their surroundings. (This is especially evident in the map of LSR velocity in Fig. 1.)

The only notable inconsistency between the fits in Table 4 and the Goodman et al. (1993) results concerns L1495NW. A bad point was found in the original data file used to calculate the gradient in L1495NW, which means that the current fit results *for that core* are more reliable than the results published earlier.

For the dense cores (or the individual clumps in the case of L1495), we see that β ranges between about 0.001 and 0.03. For the L1495 complex, $\beta = 0.13$, which is significantly greater than that for its individual clumps. It would seem that the orbital clump-clump motion within a double core region like L1495 contributes significantly more to the gradient than the spin of the individual clumps. Similar behavior is apparent in the L1251 complex, where NH₃ maps of L1251A and L1251E (a nearby core in the same dark cloud) have nearly orthogonal gradients, while the clump-to-clump NH₃ gradient direction agrees very well with that in the environmental gas traced by C¹⁸O observations (see Goodman et al. 1993). It would appear that cores spin along an axis that is not easy to predict (i.e., it is not aligned in an obvious way with their elongation), but they “orbit” each other in a reference frame fixed to their environment. Perhaps it is best to think of them as independently spinning test particles in a turbulent sea.

⁷ The densities used in estimating β are for the nearest core listed in Benson & Myers (1989). These densities are measured at only one position and are not necessarily applicable “averages” for each region studied. As a result, the β values listed should be considered uncertain by factors of ~ 2 -3.

5. SUMMARY AND DISCUSSION

5.1. Summary

Within the half-power contours of NH₃ maps of dense cores, we find that the spectral line width is roughly *constant* at a value slightly higher than the thermal limit, whereas at the edges of the NH₃ maps, the line width appears to slightly increase.

In order to come to this result, it was necessary to take the following four steps:

1. Construct NH₃ maps to very high sensitivity levels in order to achieve dynamic range in $T_A^* \sim 10$.
2. Derive an intrinsic line width for the spectrum at each position. In high S/N spectra, this is achieved by simultaneous fitting of the 18 components of the NH₃ hyperfine spectrum. In lower S/N cases, the intrinsic widths are estimated via a conversion algorithm (see Appendix A) which uses the width of the main hyperfine blend and an estimate of the optical depth as inputs. The input optical depths are estimated using a $\tau_0(T_A^*)$ relation derived empirically from the measured optical depths and antenna temperatures for the high S/N points in each map.
3. Take T_A^* as a proxy for size scale in an individual core, and empirically derive a $T_A^*(R)$ relation. We find that $T_A^* \propto R^{-1}$ for most cores (see Appendix B).
4. After taking these three steps, display scatter plots of line width versus antenna temperature. These plots indicate that the line width within the half-power contour of an NH₃ core is nearly independent of position and has a value that is significantly suprathemal.

In order for the constant line widths typically measured within the half-power contour of dense cores to originate in thermal gas, its kinetic temperature would need to be $T_K \sim 30$ K, which is about 3 times the measured T_K . Therefore, we conclude that *some residual nonthermal (i.e., turbulent or wavelike) motions remain inside R_{coh}* in dense cores, but that they are different in nature (e.g., subsonic vs. supersonic) from the nonthermal motions on larger scales (see Paper II) in that their magnitude does not measurably depend on size scale.⁸ The magnitude of these residual nonthermal line

⁸ In Paper II, we consider how pathological distributions of the NH₃ molecules in a core can cause line width to appear independent of size scale. Specifically, a shell-like geometry can give this result, but careful studies of the NH₃ distribution in cores (Kuiper, Langer, & Velusamy 1996) indicate that NH₃ is one of the *least* depleted dense gas tracer molecules in core interiors and thus that it should trace more of a filled volume than a shell.

widths (typically $\Delta v_{\text{NT}} < 0.2 \text{ km s}^{-1}$) is always less than the thermal line width of H_2 at 10 K ($\Delta v_T = 0.44$), which means that any turbulence within coherent cores is subsonic. One might wonder why even subsonic turbulence would appear scale-independent. This is a good question, but we fear that the dynamic range of our data on scales smaller than R_{coh} is not large enough to absolutely rule out *any* scale dependence of these residual motions. We can only say that the scale-dependence of the nonthermal motions associated with dense cores is much stronger on larger scales than small scales, and we speculate that this transition is caused by a change in the nature of the turbulent motions (see § 5.2).

Interpretation of the velocity gradients in dense cores and their environs as rotation indicates that the cores spin independently of their surroundings, along an axis not obviously related to their shape. Comparison of gradients implied by the relative velocities of high-density cores in complexes and gradients in the extended low-density gas in these complexes suggests a picture in which the cores behave as (independently spinning) test particles, floating along in a turbulent flow.

5.2. Speculation and a “Coherence” Scenario

On large (1–100 pc) scales, molecular clouds are supported against gravitational collapse by primarily nonthermal (turbulent, wavelike) motions. On the small (~ 0.1 pc) scales associated with star formation, thermal pressure becomes a significant contributor to cloud support. How is this transition accomplished? The turbulent support must be diminished on smaller scales, either through random fluctuations or dissipation—or both. It is possible that cores originate in randomly occurring regions of reduced turbulent support—e.g., eddies—in which gravity gets a better chance at dominating turbulent and other kinetic pressures. Alternatively, it is also possible that these regions of reduced turbulence represent an “inner scale” of a turbulent cascade initiated on larger scales (e.g., as suggested by Kleiner & Dickman 1987).

However these coherent regions occur, it seems likely that the gravitational collapse necessary to form a protostar is seeded in them, and then allowed to proceed via ambipolar diffusion (Mestel & Spitzer 1956; Mouschovias 1978, 1987a, 1987b; Shu, Adams, & Lizano 1987). Myers & Goodman (1988b) have shown that ambipolar diffusion is most efficient on size scales similar to R_{coh} , ~ 0.1 pc, for magnetic field strengths typical of cores (15–40 μG). In Paper II, we discuss what physical processes might select scales $R_{\text{coh}} \sim 0.1$ pc as characteristic of the transition to coherence. The scale at which the turbulent or wavelike magnetic field decouples from the neutral gas high-density cores is a leading contender.

Previous work has also hinted at a coherence length ~ 0.1 pc in dark cloud/dense core regions. In the fourth paper of their pioneering series of papers on using autocorrelation analyses to interpret the velocity field in dark clouds, Kleiner & Dickman (1987) find a correlation length ~ 0.1 pc in ^{13}CO maps of the Heiles cloud 2 region of Taurus, along with a “rapid increase in coherence on scales smaller than the correlation length.” However, Miesch & Bally (1994) might disagree with Kleiner & Dickman’s conclusions. Miesch & Bally applied the same sort of autocorrelation function (ACF) and structure function (SF) analysis techniques that were first applied to molecular line maps by Scalo (1984), and then used by Kleiner & Dickman, to their own extensive set of ^{13}CO observations and to simulated data that had no intrinsic correlation length. Based primarily on analysis of the simulation, they conclude that false correlation lengths ~ 2 or 3 beams in size can be produced—by effects related to the finite beam size—in the ACF and SF analyses. Kleiner & Dickman’s beam corresponds to 0.04 pc, which is 2.5 times smaller than the correlation length they deduce.

5.3. Future Tests of the Coherence Scenario

If cores represent the starting point of a coherent regime, then we might expect that line width actually increases with size at the edges of our maps, where the nonthermal component begins to dominate. From our current maps, it is very hard to claim unequivocal evidence of such an increase. Since strong excitation of the $(J, K) = (1, 1)$ NH_3 transition requires densities greater than 10^4 cm^{-3} and given that the density structure of dense cores is relatively steep, with

$$n = 194(r/\text{pc})^{-1.6} \text{ cm}^{-3} \quad (10)$$

(Fuller & Myers 1992), it will be extremely difficult to extend the single-tracer, single-cloud (Type 4) line width–size relations to larger size scales (but we will keep trying!). Rather than searching for this very weak emission, it is easier (see Paper II) to observe a molecular transition that traces slightly lower densities, such as C^{18}O or OH , and then compare the properties of Type 4 relations measured in a variety of density tracers. We urge the reader to continue on to Paper II to see what happens when such relations are compared!

We would like to thank Jon Arons, Paola Caselli, Charles Gammie, Mark Heyer, Ned Ladd, Richard Larson, Chris McKee, Phil Myers, Eve Ostriker, Frank Shu, Enrique Vasquez-Semadeni, Steve Stahler, David Wilner, and an anonymous referee for useful comments on this work as it was evolving.

APPENDIX A

The technique we used to simulate ammonia spectra is based on the methods employed by Pauls et al. (1983), Bachiller et al. (1987), and Benson & Myers (1989). The antenna temperature T_A^* as a function of velocity v of the $(J, K) = (1, 1)$ transition of NH_3 is modeled by

$$T_A^*(v) = \Phi \{1 - \exp[-\tau(v)]\}, \quad (11)$$

$$\tau(v) = \sum_{j=1}^{18} \alpha_j \tau_0 \exp \left\{ -4 \ln 2 \left[\frac{v - (v_j + v_0)}{\Delta v_{\text{int}}} \right]^2 \right\}, \quad (12)$$

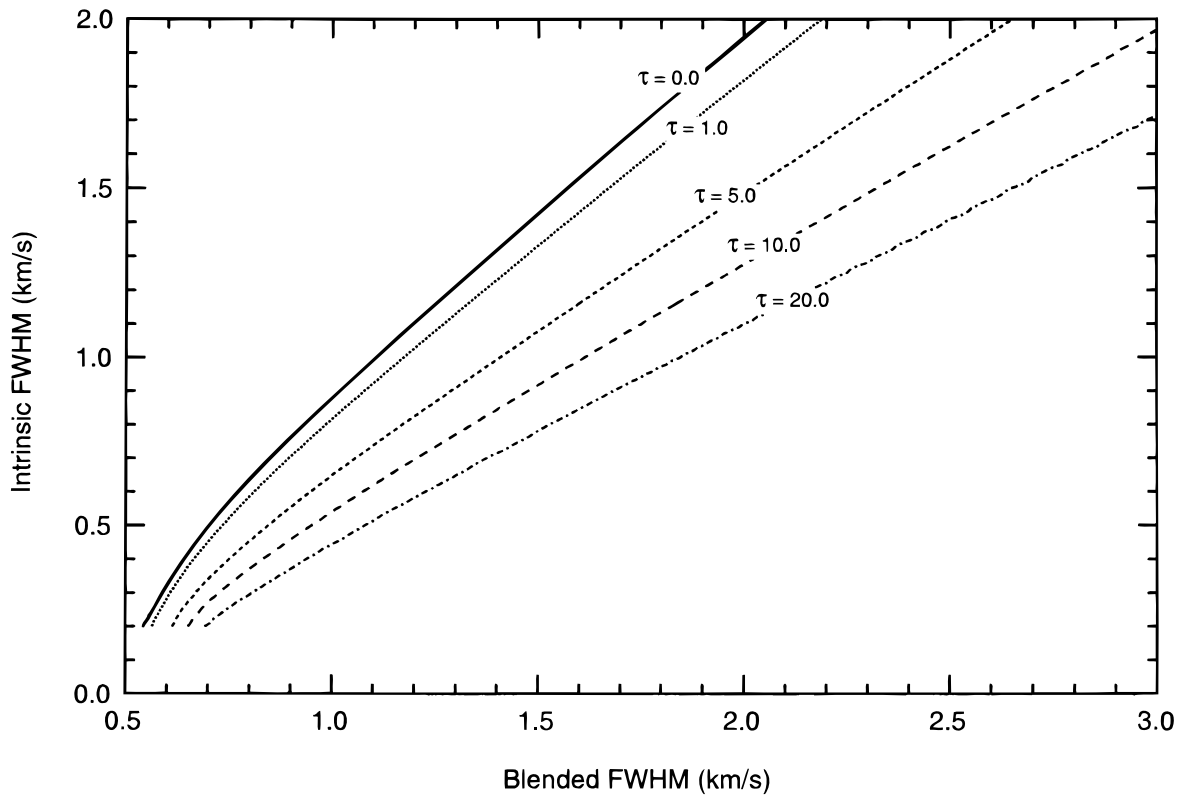


FIG. 5.—Intrinsic line width Δv_{int} vs. blended line width Δv_{blend} and total optical depth τ_0

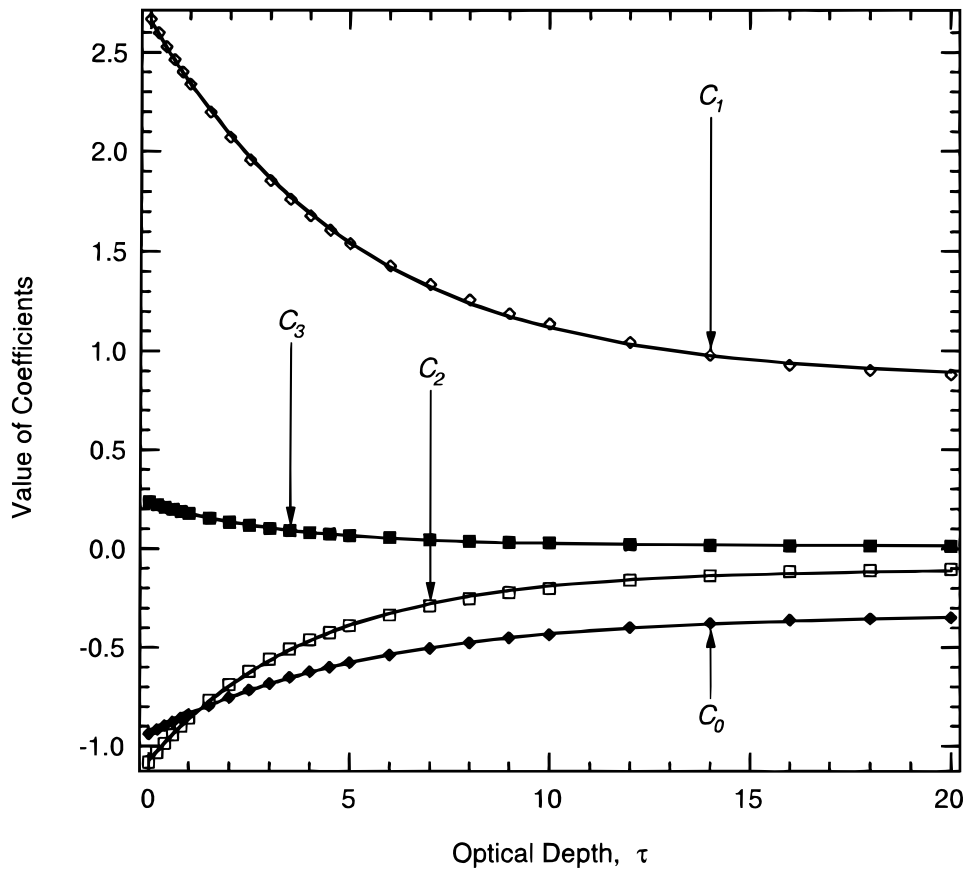


FIG. 6.—Polynomial coefficients C_n as a function of total optical depth τ_0 . Solid curves are best-fit exponentials.

where Φ is an amplitude scaling factor, α_j is the relative intensity, v_j is the velocity of the j th hyperfine component (Kukolich 1967), τ_0 is the total optical depth of the line, v_0 is the central velocity of the line, and Δv_{int} is the intrinsic line width (FWHM) of each component. For each simulated spectrum, we use a velocity resolution equal to a tenth of the intrinsic line width, so that spectral resolution effects can be neglected.

Ammonia spectra for optical depths τ_0 between 0.0 to 1.0 at intervals of 0.2, 1.0 to 5.0 at intervals of 0.5, 5.0 to 10.0 at intervals of 1.0, and 10.0 to 20.0 at intervals of 2.0 and for intrinsic line widths Δv_{int} between 0.2 and 3.0 km s^{-1} at intervals of 0.02 km s^{-1} were simulated by the above method. Single Gaussians were fit to the main blends consisting of the central eight hyperfine components. The results are graphed in Figure 5.

To extract an empirical relation from the simulated spectra, we fit a third-order polynomial to each curve in Figure 5, generating a set of polynomial coefficients $C_n(\tau_0)$ for each value of τ_0 :

$$\Delta v_{\text{int}} = \sum_{n=0}^3 C_n(\tau_0) \Delta v_{\text{int}}^n. \quad (13)$$

The values of these coefficients are graphed versus τ_0 in Figure 6. These curves are well fit by exponential functions of the form

$$C_n(\tau_0) = K_{n0} + K_{n1} \exp(-K_{n2} \tau_0). \quad (14)$$

The values of the best-fit exponential coefficients K_{nm} can be found in Table 3. The utility of this empirical relation is apparent: with an estimate of the total optical depth of the line, one can easily convert a blended line width to an intrinsic line width.

There are two types of errors that must be considered. First, the empirical relation deviates from the simulated data no more (and typically much less) than 0.04 km s^{-1} . Second, and more important, statistical uncertainties in the blended line width and in the optical depth are propagated into the uncertainty in the intrinsic line width (see, e.g., Bevington 1969). The polynomial coefficients $C_n(\tau_0)$, however, are not strong functions of optical depth; in general, a 33% uncertainty in τ_0 results in no more than (and typically much less than) a 10% uncertainty in Δv_{int} . The largest contribution to the error in the intrinsic line width is the error in the blended line width; a 5% error in Δv_{blend} typically results in a 10% error in Δv_{int} .

APPENDIX B

It is often difficult to unambiguously define a radius to a given point in a spectral line map from the peak of the map, since many dense cores are not circular in projection or have multiple emission peaks. In this appendix, we will show that the reciprocal of antenna temperature scales roughly with radius, and hence antenna temperature can be used as a substitute for size scale.

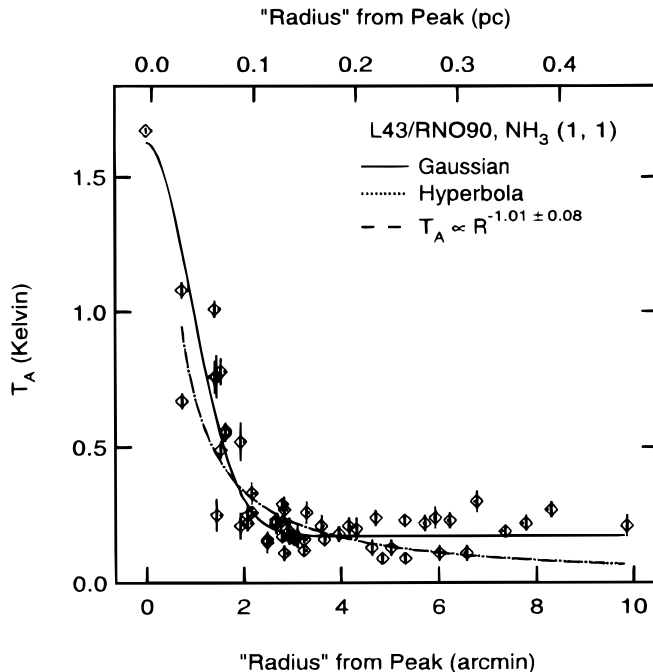


FIG. 7a

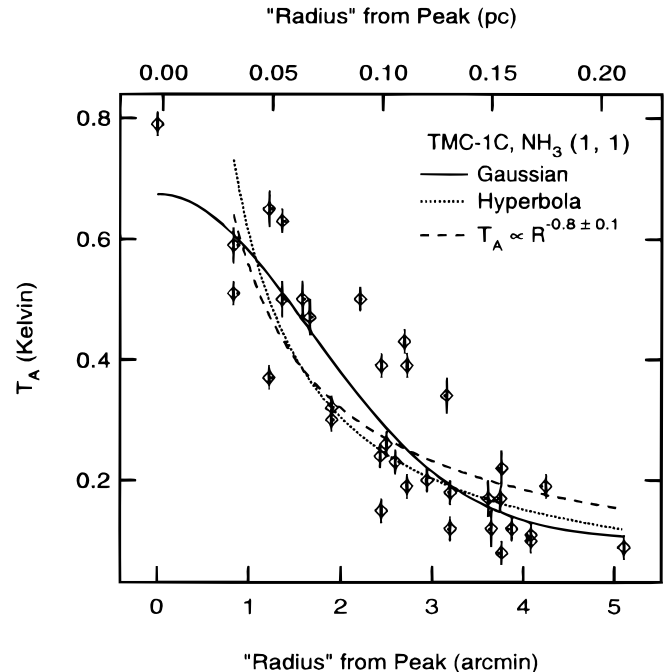


FIG. 7b

FIG. 7.—Antenna temperature T_A^* vs. radius: (a) L43/RNO 90 and (b) TMC-1C. Error bars indicate uncertainties. Solid curves are the best-fit Gaussian, dotted curves are the best-fit hyperbola, and dashed curves are the best-fit power law.

If a dense core has only one peak and is circular in projection, the radius to an arbitrary point in the map can simply be defined as $r = (\Delta\alpha^2 + \Delta\delta^2)^{1/2}$, where $\Delta\alpha$ and $\Delta\delta$ are the right ascension and declination offsets, respectively, from the peak of the map. If the projection is not circular but elliptical, we need to modify this definition of radius slightly. Rather than right ascension and declination, a more natural set of axes is a pair of axes aligned along the major and minor axes of an ellipse. Now, instead of using concentric circles to define radii, we can use concentric ellipses. We define the radius of an ellipse as the geometric mean of the semimajor and semiminor axes (respectively, a and b) of the ellipse: $r = (ab)^{1/2}$. This is equivalent to finding the radius of a circle with the same area as the ellipse. This is also equivalent to rescaling the axes so that the ellipse becomes a circle. Hence, the radius to an arbitrary point in the map is given by

$$r = \sqrt{\gamma^{-1} \Delta\alpha^2 + \gamma \Delta\delta^2}, \quad (15)$$

where γ is the axial ratio of the dense core, and $\Delta\alpha$ and $\Delta\delta$ are offsets along the major and minor axes, respectively, from the peak of the map. Figure 7 shows graphs of antenna temperature T_A^* versus radius, as defined above, for TMC-1C and L43/RNO 90. These two cores were chosen since they have only one peak and are elliptical in projection. What is typically done to model cores is to fit a Gaussian to the profile. However, as we can see in the plots, a power law and a hyperbola fit the profiles just as well. In particular, for points not including the peak, we see that $T_A^* \sim r^{-1}$ is a rough approximation to the profile and is certainly no worse a fit than a Gaussian.

In cores that are not elliptical or for cores that have more than one peak, antenna temperature is a less unambiguous indicator of the profile of the core, since a physical radius is not well defined for these cases.

REFERENCES

- Arons, J., & Max, C. E. 1975, *ApJ*, 196, 77
 Bachiller, R., Guilloteau, S., & Kahane, C. 1987, *A&A*, 173, 324
 Barrett, A., Meeks, M., & Weinreb, S. 1964, *Nature*, 202, 475
 Beichman, C. A., Myers, P. C., Emerson, J. P., Harris, S., Mathieu, R. D., Benson, P. J., & Jennings, R. E. 1986, *ApJ*, 307, 337
 Benson, P. J., & Myers, P. C. 1989, *ApJS*, 71, 89
 Bevington, P. R. 1969, *Data Reduction and Error Analysis for the Physical Sciences* (New York: McGraw-Hill)
 Caselli, P., & Myers, P. C. 1995, *ApJ*, 446, 665
 Dame, T. M., Elmegreen, B. G., Cohen, R. S., & Thaddeus, P. 1986, *ApJ*, 305, 892
 Forveille, T., Guilloteau, S., & Lucas, R. 1989, *CLASS Manual*, Version 4.0
 Fuller, G. A., & Myers, P. C. 1992, *ApJ*, 384, 523
 Gammie, C. F., & Ostriker, E. C. 1996, *ApJ*, 466, 814
 Gammie, C. F., Stone, J., & Ostriker, E. C. 1998, in preparation
 Goodman, A. A., Barranco, J. A., Wilner, D. J., & Heyer, M. H. 1998, *ApJ*, 504, 223 (Paper II)
 Goodman, A. A., Benson, P. J., Fuller, G. A., & Myers, P. C. 1993, *ApJ*, 406, 528
 Heyer, M. H., & Schloerb, F. P. 1997, *ApJ*, 475, 173
 Kitamura, Y., Sunada, K., Hayashi, M., & Hasegawa, T. 1993, *ApJ*, 413, 221
 Kleiner, S. C., & Dickman, R. L. 1987, *ApJ*, 312, 837
 Kuiper, T. B. H., Langer, W. D., & Velusamy, T. 1996, *ApJ*, 468, 761
 Kukolich, S. G. 1967, *Phys. Rev.*, 156, 83
 Landman, D. A., Rousell-Dupré, R., & Tanigawa, G. 1982, *ApJ*, 261, 732
 Larson, R. B. 1981, *MNRAS*, 194, 809
 Leung, C. M., Kutner, M. L., & Mead, K. N. 1982, *ApJ*, 262, 583
 Martin, R. N., & Barrett, A. H. 1978, *ApJS*, 36, 1
 McKee, C. F., & Zweibel, E. G. 1995, *ApJ*, 440, 686
 Mestel, L., & Spitzer, L., Jr. 1956, *MNRAS*, 116, 505
 Miesch, M. S., & Bally, J. 1994, *ApJ*, 429, 645
 Mouschovias, T. Ch. 1978, in *Protostars and Planets*, ed. T. Gehrels (Tucson: Univ. of Arizona Press), 209
 ———. 1987a, in *Physical Processes in Interstellar Clouds*, ed. G. Morfill & M. Scholer (Dordrecht: Reidel), 453
 ———. 1987b, in *Physical Processes in Interstellar Clouds*, ed. G. Morfill & M. Scholer (Dordrecht: Reidel), 491
 Myers, P. C. 1983, *ApJ*, 270, 105
 Myers, P. C., & Benson, P. J. 1983, *ApJ*, 266, 309
 Myers, P. C., & Fuller, G. A. 1992, *ApJ*, 396, 631
 Myers, P. C., & Goodman, A. A. 1988a, *ApJ*, 326, L27
 ———. 1988b, *ApJ*, 329, 392
 Myers, P. C., Ho, P. T. P., Schneps, M. H., Chin, G., Pankonin, V., & Winnberg, A. 1978, *ApJ*, 220, 864
 Pauls, T. A., Wilson, T. L., Bieging, J. H., & Martin, R. N. 1983, *A&A*, 124, 23
 Scalo, J. M. 1984, *ApJ*, 277, 556
 Scoville, N. Z., Sanders, D. B., & Clemens, D. P. 1986, *ApJ*, 310, L77
 Shu, F. H. 1995, in *Molecular Clouds and Star Formation*, ed. C. Yuan & J. You (Singapore: World Scientific), 97
 Shu, F., Adams, F. C., & Lizano, S. 1987, *ARA&A*, 25, 23
 Snell, R. L. 1981, *ApJS*, 45, 121
 Solomon, P. M., Rivolo, A. R., Barrett, J., & Yahil, A. 1987, *ApJ*, 319, 730
 Torrelles, J. M., Rodriguez, L. F., Cantó, J., Carral, P., Marcaide, J., Moran, J. M., & Ho, P. T. P. 1983, *ApJ*, 274, 214
 Zweibel, E. G., & Josafatsson, K. A. 1983, *ApJ*, 270, 511